Editors' Suggestion

Ubiquity of amplitude-modulated magnetic ordering in the H-T phase diagram of the frustrated non-Fermi-liquid YbAgGe

C. B. Larsen [1] E. Canévet,[1] D. G. Mazzone,[1] Ch. Rüegg,[1,2,3] B. Fåk,[4] D. F. McMorrow,[3] E. Ressouche,[5]
G. J. McIntyre [4,*] S. L. Bud'ko,[6] P. C. Canfield [6] and O. Zaharko[1,†]

[1]*Laboratory for Neutron Scattering and Imaging, Paul Scherrer Institute, CH-5232 Villigen, Switzerland*
[2]*Department of Quantum Matter Physics, University of Geneva, CH-1211 Geneva, Switzerland*
[3]*London Centre for Nanotechnology and Department of Physics and Astronomy, University College London,
London WC1E 6BT, United Kingdom*
[4]*Institut Laue-Langevin, 71 Avenue des Martyrs, CS20156, 38042 Grenoble Cédex 9, France*
[5]*University Grenoble Alpes, CEA, IRIG, MEM, MDN, 38000 Grenoble, France*
[6]*Ames Laboratory and Department of Physics and Astronomy, Iowa State University, Ames, Iowa 50010, USA*

YbAgGe contains a magnetic geometrically frustrated kagome-like lattice that also features significant local single-ion anisotropy. The electronic state is established by hybridization of $4f$ and conduction electrons leading to heavy electronic masses. The competition between these various interactions leads to nontrivial behavior under external magnetic field, including a sequence of magnetic phase transitions, non-Fermi-liquid states, and possibly a quantum critical point. We present a series of neutron diffraction experiments performed in the mK temperature range and under magnetic fields up to 8 T in the hexagonal plane, revealing the microscopic nature of the first four subsequent magnetic states of this phase diagram. The magnetic phases are associated with the propagation vectors $\mathbf{k_1} = (\frac{1}{3}\ 0\ \frac{1}{3})$ for $H < 2$ T, $\mathbf{k_2} = (0\ 0\ 0.32)$ for 2 T $< H < 3$ T, $\mathbf{k_1} = (\frac{1}{3}\ 0\ \frac{1}{3})$ for 3 T $< H < 4.5$ T, and $\mathbf{k_3} = (0.195\ 0.195\ 0.38)$ for 4.5 T $< H < 7$ T. Our structural refinements reveal a strong modulation of the magnetic moment amplitude in all phases. We observe that the ordered moments of the three magnetically different Yb sites become increasingly different in field, which complies with the principle local anisotropy directions relative to the field direction. While the ordered moments are aligned predominantly in the hexagonal plane, we also find a significant out-of-plane component and a ferromagnetic contribution above 2 T. We discuss possible scenarios that may evolve around the phase boundary at 4.5 T, which is associated with putative quantum criticality as identified by various bulk probes. We propose further steps that are required to better understand the microscopic interactions in this material.

I. INTRODUCTION

Several topical themes of modern solid-state research—frustrated magnetism, non-Fermi-liquid behavior, and field-induced quantum criticality—converge in YbAgGe, a system that has been in the focus of experimental studies for more than a decade [1–12].

YbAgGe belongs to a family of rare-earth (R) compounds with noncentrosymmetric crystal structure (ZrNiAl-type, space group $P\bar{6}2m$), where the R^{3+}-ions occupy the $3(f)$ Wyckoff position (C_{2v} site symmetry) and form a two-dimensional, distorted kagome-like lattice of corner-sharing equilateral triangles [13]. Some members of this family, i.e., TbPtIn and TmAgGe [14,15], possess a very strong easy-axis anisotropy in the hexagonal plane, which is imposed by the crystal-electric field (CEF). This leads to a susceptibility ratio of $\chi_{ab}/\chi_c \approx 30$ at 5 K, and triggers a series of metamagnetic transitions in which the magnetic moments are restricted along the three distinct axes defined by the CEF, and which are selected by the magnetic field direction [15]. The sister compound HoAgGe features a kagome spin-ice state that is established through the combination of single-ion axial anisotropy in the hexagonal plane and effective ferromagnetic nearest-neighbor exchange interactions [16]. Under field this state evolves into ordered and partially disordered magnetic states, all obeying the kagome ice rule.

The magnetic moments in YbAgGe also show axial anisotropy within the hexagonal plane, but here they couple antiferromagnetically. The material features a Curie-Weiss temperature of $\theta_{CW} = -30$ K and an anisotropy ratio that reaches moderate $\chi_{ab}/\chi_c \approx 3$ at low temperature [14]. Inelastic neutron scattering (INS) results suggest a doubly degenerate CEF ground state $|J = 7/2, J_z = \pm 7/2\rangle$ [9]. The local quantization axis for the three magnetic Yb sites of the unit cell [Yb1 = (x,0,0), Yb2 = (0,x,0), Yb3 = (−x,−x,0), x = 0.58] points along the $z = [1\ 0\ 0]$, $[0\ 1\ 0]$, or the $[1\ 1\ 0]$ two-fold axes, respectively. Thus the anisotropy is essentially the same as in the TmAgGe [14] member of the RAgGe family as well as the isostructural TbPtIn [14].

*Present address: Australian Nuclear Science and Technology Organisation, Lucas Heights NSW 2234, Australia.
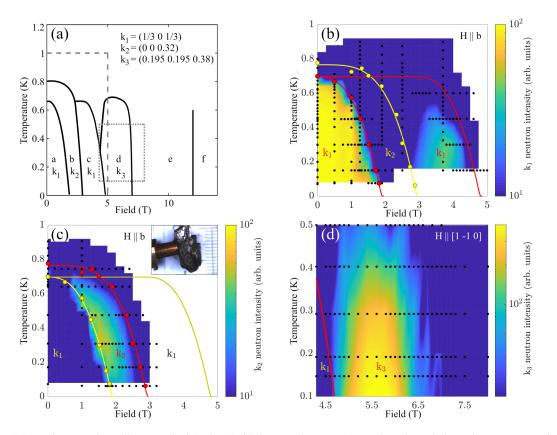†oksana.zaharko@psi.ch

FIG. 1. (a) Schematic *H*-*T* phase diagram of YbAgGe. Solid lines mark approximate phase boundaries. [(b), (c)] Maps of the magnetic intensity for selected reflections corresponding to $\mathbf{k_1}$ and $\mathbf{k_2}$ propagation vectors, respectively [see also dashed region in (a)]. (d) Map of the magnetic intensity for $\mathbf{k_3}$ in the dotted region of panel (a). The yellow and red lines indicate the approximate magnetic phase boundaries, while black dots indicate the exact measurement points. The magnetic field was applied along the $\hat{b}$ direction in (b) and (c) and along [1 −1 0] in (d). The inset in (c) shows a $14 \times 8 \times 8$ mm^3 YbAgGe single crystal on a copper mount.

Low-temperature thermodynamic and transport results [1–5,14,17,18] distinguish YbAgGe from other RAgGe compounds with well localised R moments. The electronic specific-heat coefficient γ ranges from 0.15 to 1 J/molK^2 and the entropy release is only ∼5% of Rln2 at 1 K [1,3,14]. This signifies that YbAgGe may be on the border of magnetic moment formation, which is established through hybridization between $4f$ and conduction electrons. Specific-heat and resistivity measurements under magnetic field and mK temperatures suggest non-Fermi-liquid behavior and quantum-critical fluctuations at the field values of $H_{\mathrm{crit}}^{ab} \approx$ 4.5 T and $H_{\mathrm{crit}}^{c} \approx$ 8 T for field directions in the hexagonal plane and along the c axis, respectively [1,3,5,7,12].

The complex *H*-*T* phase diagram of YbAgGe [Fig. 1(a)], constructed from detailed bulk measurements [1–5,14,17,18], contains up to six different phases labeled by the letters *a* to *f* [5]. Earlier magnetic neutron elastic-scattering studies were able to identify the ordering wave vectors of the first two of these phases. At zero field the magnetic Yb^{3+} moments order below 0.65 K along the wave vector $\mathbf{k_1} = (\frac{1}{3}\, 0\, \frac{1}{3})$ (phase *a*) [8]. Phase *b* features the incommensurate wave vector $\mathbf{k_2} = (0\, 0\, 0.32)$ [10] and encapsulates the phase *a* in the *H*-*T* phase diagram. It extends up to $T_N \approx 0.8$ K at zero field, after which magnetic order vanishes. At low temperatures ($T < 0.65$ K), phase *b* exists within 2 T $< H <$ 3 T.

The magnetic order of the higher-field phases *c*, *d*, and *e* have remained elusive to this date. However, the $c − d$ phase

boundary has been intensively studied because of numerous anomalous properties. The Hall resistivity is enhanced [2], the sign of the Grüneisen parameter changes [7], the magnetization peaks [19], and the elastic constants soften [6]. Detailed magnetocaloric measurements [7] classify the sharp transition at $T_{BCP} \approx 0.3$ K and $H_{BCP} \approx 4.5$ T as a bicritical point (BCP), which may be tuned to become quantum critical.

Thus, the evolution of the field-induced magnetic structures in YbAgGe, especially the ones for phases *c* and *d*, is indispensable for our understanding of the complex interplay between the geometrical frustration of Yb^{3+} moments on the kagome-like lattice, their local orthorhombic CEF anisotropy, and their interaction with the conduction electrons. Here we report neutron diffraction experiments on YbAgGe single crystals in zero and applied magnetic fields. We identify the corresponding propagation vectors and determine the magnetic structures of all four successive states *a*, *b*, *c*, and *d*.

II. EXPERIMENTAL DETAILS

A. Sample preparation

YbAgGe single crystals were grown from Ag- and Ge-rich high-temperature ternary solutions and characterized based on the procedure described in Ref. [14]. In order to grow a significant number of large single crystals of YbAgGe, the growth was optimized in several ways.

Roughly 10 g of high-purity Yb, Ag, and Ge were placed in a 5 ml Al_2O_3 crucible in a molar ratio of $Yb_{0.14}Ag_{0.645}Ge_{0.215}$. The Yb with 99.99+% purity was obtained from the Ames Laboratory Materials Preparation Center. A second 5 ml Al_2O_3 crucible, filled with silica wool, was placed on top of the growth crucible to act as a filter and catch for excess liquid [20]. The growth and catch crucibles were sealed into an evacuated amorphous silica tube and placed in a resistively heated box furnace. The furnace was heated to 1100 °C over 4 hours, and heated further to 1190 °C over an additional hour. The furnace was then cooled to 1090 °C over 5 hours and then slow cooled to 840 °C over 200 hours. The growth crucibles were removed from the furnace at 840 °C and placed in a centrifuge for separation of the excess liquid from the YbAgGe single crystals. Depending on nucleation, single crystals as large as 1–2 grams could be obtained [see inset to Fig. 1(c) for an example].

B. Neutron diffraction setups

A series of neutron-diffraction experiments was performed on the single-crystal neutron diffractometers D10 and D23 at the Institut Laue-Langevin (ILL), France, and on the single-crystal neutron diffractometer Zebra (former TriCS) at the Swiss Neutron Spallation Source SINQ, Paul Scherrer Institut (PSI), Switzerland.

D10 was operated with a wavelength of 2.36 Å in four-circle mode with a dilution refrigerator at 140 mK in zero magnetic field. The Zebra (TriCS) and D23 experiments used neutron wavelengths of 2.43 Å and 2.366 Å, respectively. The last two diffractometers were operated with lifting-arm normal-beam geometry and were equipped with dilution refrigerators inserted into vertical magnets. For the study of the H-T phase diagram, the YbAgGe crystals were mounted and cooled to a base temperature of 60 mK on Zebra (TriCS) and D23. The field was applied in the hexagonal plane, either along [1 –1 0] or along the $\hat{b}$ axis. According to bulk measurements [3,9], the essential features of the phase diagram remain unchanged for these different field directions, but the

phase boundaries may slightly shift. A consistent zero-field cooling protocol was used in all experiments, i.e., after each field ramp the crystal was heated to 1 K and cooled in zero field to base temperature. Data sets for the three field-induced phases were collected at magnetic fields of 2.2 T, 3.9 T, and 5.5 T applied along $H_{1\bar{1}0}$. Our neutron-diffraction experiments reveal that magnetic reflections occurring in phases a, b, c, and d [Fig. 1(a)] can be indexed with the propagation vectors $\mathbf{k_1}$ [Fig. 1(b)], $\mathbf{k_2}$ [Fig. 1(c)], $\mathbf{k_1}$ [Fig. 1(b)], and $\mathbf{k_3}$ [Fig. 1(d)], respectively. The a phase with propagation vector $\mathbf{k_1}$ is separated from the other phases by a first-order transition, and shows a clear hysteresis. Meanwhile, the phase transition of phase b is second order when approached from high temperature or field, but is first order when entered from the a-phase. We observed weak intensities at the $\mathbf{k_1}$ positions that coexist with the $\mathbf{k_2}$ reflections in the b phase, suggesting a competition between these two magnetic states. Magnetic Bragg reflections at $\mathbf{k_1}$ reappear in the c phase, albeit with a different domain population and moment direction when compared to the zero-field state (see further below). The propagation vector $\mathbf{k_3}$ of the d phase was found by extensive reciprocal (hhl)-plane mapping.

We also searched for new propagation vectors in the e phase by mapping the reciprocal (h0l) plane from (0.25 0 0) to (0.87 0 1) and the (hhl) plane from (0.1 0.1 0) to (0.7 0.7 1) at 8 T. However, no magnetic signal was found.

C. Exploration of the phase diagram

Figure 2 presents the field evolution of the antiferromagnetic reflections $(\frac{1}{3} \; -\frac{1}{3} \; \frac{1}{3})$, (1 0 0.32), and (0.195 0.195 0.62) alongside the magnetic contribution to the nuclear (110) Bragg peak. The different slopes of rising and decreasing intensities at various phase boundaries suggest possible crossovers from second- to first-order transitions, which is in agreement with magnetization, dilation and thermopower results [4,5,14,17,19]. The magnetic contribution to (110) sets in at the b phase and continues to rise with a similar
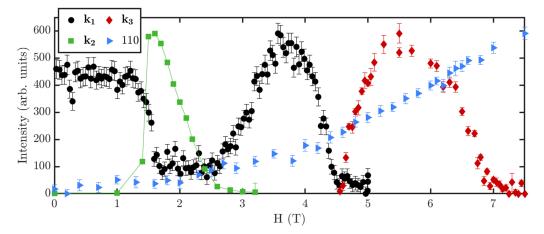

FIG. 2. Field dependence of the $(\frac{1}{3} \; -\frac{1}{3} \; \frac{1}{3})$ ($\mathbf{k_1}$) and (0.195 0.195 0.62) ($\mathbf{k_3}$) magnetic Bragg peaks overplotted with the nuclear (110) Bragg intensity, measured with increasing field $H_{[1\bar{1}0]}$ at base temperature. The plot also includes the field dependence of the magnetic (1 0 0.32) ($\mathbf{k_2}$) Bragg peak measured with the field along the $\hat{b}$ axis. The intensities with different colours have been measured in different experiments and have been rescaled to the same maximum intensity. Thus they are not directly comparable.

TABLE I. The arms of each propagation vector **k** ($-$**k** arms are not listed explicitly) and the overview of the data sets measured at four magnetic fields. ✓ and – denote data sets with significant and negligible intensity, respectively. The number of reflections considered for the magnetic structure refinement is given in brackets.

k	**k**^{arm}	H(T)			
		0	2.2	3.9	5.5
k$_1$	$(\frac{1}{3}\ 0\ \frac{1}{3})$	✓		–	
	$(-\frac{1}{3}\ \frac{1}{3}\ -\frac{1}{3})$	✓		✓ (111)	
	$(0\ \frac{1}{3}\ \frac{1}{3})$	✓		–	
	$(0\ \frac{1}{3}\ -\frac{1}{3})$	✓ (127)		–	
	$(\frac{1}{3}\ -\frac{1}{3}\ -\frac{1}{3})$	✓		✓	
	$(\frac{1}{3}\ 0\ -\frac{1}{3})$	✓		–	
k$_2$	(0 0 0.32)		✓ (96)		
k$_3$	(0.195 0.195 0.380)				✓ (92)
	(–0.390 0.195 –0.380)				–
	(0.195 –0.390 0.380)				–
	(0.195 –0.390 –0.380)				–
	(0.195 0.195 –0.380)				✓ (92)
	(–0.390 0.195 0.380)				–

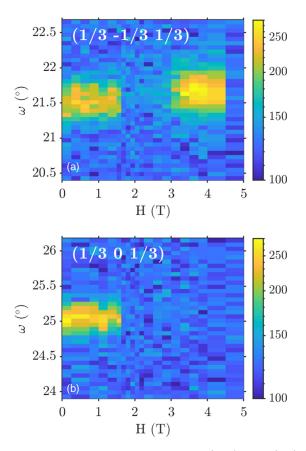

FIG. 3. Field evolution of the magnetic $(\frac{1}{3}\ 0\ \frac{1}{3})$ and $(\frac{1}{3}\ -\frac{1}{3}\ \frac{1}{3})$ reflections for $H||[1\bar{1}0]$. The angle ω is transversal to the scattering vector.

slope through the c and d phases, which indicates complex conical moment arrangements.

D. Domain population and data sets

Each of the identified propagation vectors **k** is related to other wave vectors by symmetry operations of the paramagnetic space group. This forms a unique set, which is called the star of the propagation vector. During our experiments we extensively inspected the arms of all propagation vectors and we summarize their presence in Table I.

The field dependence of the pair of reflections $(\frac{1}{3}\ 0\ \frac{1}{3})$ and $(\frac{1}{3}\ -\frac{1}{3}\ \frac{1}{3})$, belonging to different arms of **k$_1$**, is shown in Fig. 3. The first reflection is present only in the a phase, whereas the second peak appears in both the a and c phases. Thus, the phases a and c feature the same propagation vector **k$_1$**, but a different number of arms are populated. In zero field, all twelve arms are observed, while at 3.9 T only four arms with in-plane components directed along the applied field remain populated (Fig. 4). Similarly, only four out of twelve arms reveal finite intensity in the d phase at 5.5 T. Their in-plane components are orthogonal to the field (Table I, Fig. 4). These observations may be rationalized in terms of magnetic configuration domains, which give rise to magnetic reflections of different arms. Determination of the domain population is important for refining the magnetic moment amplitude of a magnetic state.

The zero-field data set (phase a) collected on D10 contained 581 magnetic reflections belonging to all twelve arms of **k$_1$** $= (\frac{1}{3}\ 0\ \frac{1}{3})$. The intensity distribution unambiguously showed that all six configuration domains were equally populated. We used 127 reflections of the $(0\ \frac{1}{3}\ -\frac{1}{3})$ arm to determine the magnetic structure. At $H = 2.2$ T (phase b), 96 magnetic reflections with propagation vector **k$_2$** $= (0\ 0\ 0.325)$ were collected. This phase has only one configuration domain and

all reflections were used for the refinement of the magnetic structure. At $H = 3.9$ T (phase c), 443 reflections of the propagation vector **k$_1$** were measured. We used 111 reflections of
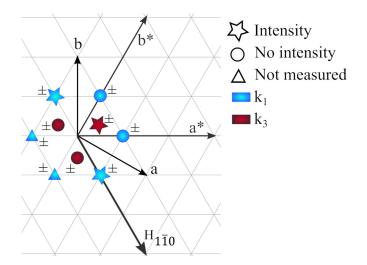

FIG. 4. Schematic view of the in-plane real-space lattice ($\hat{a}\hat{b}$), reciprocal-space lattice (a^*b^*), and projection of the in-plane components of the **k$_1$** and **k$_3$** arms for $H||[1\bar{1}0]$ at 3.9 T and 5.5 T, respectively. Reflections with components above and below the hexagonal plane are indicated by $\pm$ signs. Four of the **k$_1$** arms could not be reached due to instrumental limitations and were therefore not measured.

TABLE II. Overview of representation analysis of the three observed propagation vectors.

k	BZ point	IRR	# Orbits
k_1	$D(\alpha, 0, \gamma)$	Γ_1	3
		Γ_2	2
k_2	$DT(0,0,\gamma)$	Γ_1	1
		Γ_2	1
		Γ_3	1
k_3	$C(\alpha, \alpha, \gamma)$	Γ_1	1
		Γ_2	1

the $(-\frac{1}{3}\ \frac{1}{3}\ -\frac{1}{3})$ arm for the magnetic structure determination. At $H = 5.5$ T (phase d) 368 reflections for the star of $k_3 = (0.195\ 0.195\ 0.380)$ were measured. Only 184 reflections belonging to two configuration domains had significant intensity and 92 reflections of the $(0.195\ 0.195\ -0.380)$ arm were used for further analysis.

III. MAGNETIC STRUCTURE DETERMINATION

A. Magnetic symmetry and refinement strategy

Symmetry representation analysis is a powerful method allowing to construct the magnetic structure models according to physically irreducible representations (IRRs) of the paramagnetic space group. We performed such analysis with the program Basireps [21] for k_1, k_2, and k_3. In all three cases, k and $-k$ are not equivalent, and we considered the extended little group (k_1, $-k_1$). An overview of the basic symmetry properties of each solution is presented in Table II, while a more detailed description of the basis functions can be found in Table V. This approach is justified for second-order phase transitions and is comparable to considering only maximal subgroups. In the case of YbAgGe, some transitions are of first order, and symmetry might therefore be lower, but we decided to stay within this approximation to reduce the number of refined parameters.

The wave vector $k_1 = (\frac{1}{3}\ 0\ \frac{1}{3})$ relates to the D point of the structural Brillouin Zone (BZ), $D(\alpha, 0, \gamma)$. In our case the variables α and γ attain the rational value $\frac{1}{3}$. None of the symmetry elements of the space group $P\bar{6}2m$ leave the wave vector k_1 invariant. The little group contains only the identity in standard representation analysis, and this leads to three independent Yb atoms. As we consider the extended little group (k_1, $-k_1$), two possible irreducible representations (IRRs) result. The first IRR, Γ_1, leaves the magnetic moments of the three Yb atoms in the unit cell independent. The second one, Γ_2, couples the moments of Yb1 and Yb3 (they form one orbit), while Yb2 remains independent.

The wave vector $k_2 = (0\ 0\ 0.325)$ belongs to the DT-point of the BZ, $DT(0,0,\gamma)$. Since we consider the extended little group (k_2, $-k_2$), the magnetic moments of the three Yb atoms are related by symmetry forming one orbit. Therefore three IRRs exist.

The wave vector $k_3 = (0.195\ 0.195\ 0.38)$ is the C point of the BZ, $C(\alpha, \alpha, \gamma)$. In this case the symmetry analysis with the extended little group (k_3, $-k_3$) implies one orbit and two IRRs.

For each of the models, the modulated magnetic moment is represented as

$$\mathbf{m}_l(\mathbf{t}) = \frac{1}{2} \sum_j \left[C_j \Psi_j^l \exp(-i2\pi\mathbf{k} \cdot \mathbf{t}) \right.$$
$$\left. + \left(C_j \psi_j^l\right)^* \exp(i2\pi\mathbf{k} \cdot \mathbf{t}) \right], \quad l = 1, 2, 3, \quad (1)$$

where Ψ_j^l denotes the jth basis function of moments at site l, $\mathbf{k}$ is the propagation vector, and $\mathbf{t} = (t_a, t_b, t_c)$ is a translation vector defining the unit cell. C_j are refinement parameters that can be flagged as either real or imaginary, such that any model, including amplitude modulated ones defined by only real parameters or completely general helices defined by both real and imaginary parameters, can be considered.

To better understand the evolution of the magnetic moments with field, we introduce an orthogonal coordinate system (ξ, η, ζ) where ξ is parallel to the magnetic field direction $[1,-1,0]$, η is along $[1,1,0]$, and ζ is along $[0,0,1]$. The moment on site $l = 1\ldots 3$ in unit cell $\mathbf{t}$ can then be written

$$\mathbf{m}_l(\mathbf{t}) = m_l^H(\mathbf{t})\hat{\xi} + m_l^{[1,1,0]}(\mathbf{t})\hat{\eta} + m_l^c(\mathbf{t})\hat{\zeta}, \quad (2)$$

where m_l^H is the moment component parallel to the applied field and $m_l^\perp(\mathbf{t}) = \sqrt{[m_l^{[1,1,0]}(\mathbf{t})]^2 + [m_l^c(\mathbf{t})]^2}$.

For each magnetic phase, we attempted refinements for all symmetry-allowed structures and for all possible permutations of real/imaginary C_j flags. Parameters resulting from the best refinements for each IRR are listed in Table III, while the magnetic moment amplitudes of these structures are presented in Table IV. The determined magnetic structures are presented in Fig. 5.

B. Zero-field k_1 phase

The zero-field refinement results of Table III reveal that the best solutions for the Γ_1 and Γ_2 IRRs have similar goodness of fit and refinement parameters. This is likely a result of the high number of free parameters for both IRRs, which put only few restrictions on the magnetic moment. Therefore both IRRs are capable of approximating the experimental data well. Plots and further discussion of the zero-field model are based on parameters from the slightly better Γ_2 solution.

Figure 5(a) depicts a $\mathbf{t} = (t_a, t_b, 0)$ layer of the zero-field amplitude-modulated moment arrangement. The in-plane components of the Yb1 and Yb2 magnetic moments are aligned along the $[1\ 0\ 0]$ and $[0\ 1\ 0]$ directions, respectively, while the Yb3 moments are arranged along the diagonal $[1\ 1\ 0]$. These orientations correspond to the principal directions of the CEF anisotropy due to the orthorhombic point symmetry of the 3(f) site [9]. The maximum moment value of 2.6(1) μ_B is reduced compared to the free-ion value of 4.5 μ_B for Yb^{3+}. The average ordered moment amplitude, $\langle|\mathbf{m}_l(\mathbf{t})|\rangle$, is 1.87(4) μ_B for Yb1 and Yb3 and 1.04(4) μ_B for Yb2 (Table IV). Thus, the average moment associated with the amplitude modulated arrangement significantly exceeds the estimates of a static ordered moment of 0.1 μ_B from the magnetic entropy calculations [3]. It might well be that the correlations probed in our diffraction experiment are not entirely elastic, but contain significant

TABLE III. Refined basis-vector coefficients for selected arms. The *i*th element of each entry in the "Flags" column refers to the designation of the corresponding refinement parameter C_i as being either real or imaginary.

IRR	k_{meas}	Flags	C_1	C_2	C_3	C_4	C_5	C_6	C_7	C_8	C_9	χ^2	R_F	R_{F^2}	$R_{F^2_w}$
k_1^{arm} = (0 1/3 −1/3), *H* = 0 T															
Γ_1		011011100	−2.6(1)	0.3(2)	−1.1(3)	1.05(7)	0.28(7)	0.5(1)	−1.7(1)	−0.7(2)	0.2(2)	31.8	14.7	24.2	26.8
Γ_2		000011111	−0.7(1)	−0.17(9)	−0.7(2)	−1.2(1)	2.38(6)	−0.39(9)	−0.4(1)	0.7(1)	−0.6(2)	25.2	12.4	21.3	23.9
k_2 = (0 0 0.32), *H* = 2 T															
Γ_1		0	−1.5(1)									73.9	36.7	59.0	68.0
Γ_2		10	−1.16(5)	0.6(1)								42.6	26.3	44.6	51.2
Γ_3		000001	0.5(2)	0.9(2)	0.6(1)	−1.1(2)	−1.2(3)	0.2(2)				29.5	22.9	38.3	41.5
k_1^{arm} = (1/3 −1/3 1/3), *H* = 3.9 T															
Γ_1		111100111	−1.3(1)	−1.8(1)	−0.1(1)	0.11(6)	−0.88(5)	0.21(6)	0.6(1)	0.17(8)	−0.8(1)	4.16	11.1	19.8	17.5
Γ_1 Fix ani		001101001	0.64(6)	0	0.16(2)	1.00(4)	0.57(7)	0.16(8)	0.5(1)	0	0.3(1)	4.88	11.5	20.9	19.2
Γ_2		111100110	0.92(9)	1.2(1)	−0.5(1)	−0.4(1)	1.26(7)	1.4(1)	−0.2(1)	−0.12(5)	0.4(1)	4.19	11.1	19.6	17.6
Γ_2 Fix ani		000010101	−1.0(1)	0	−0.5(2)	−0.8(1)	1.17(9)	0	−0.4(1)	0	−0.3(2)	5.14	12.1	22.0	19.8
k_3^{arm} = (0.195 0.195 −0.38), *H* = 5.5 T															
Γ_1		0111110	0.4(1)	−0.3(1)	−0.2(1)	1.4(2)	1.6(2)	−1.1(3)	0.0(1)			23.0	15.9	28.3	28.7
Γ_2		11000000	−0.37(4)	−0.53(7)	0.08(7)	2.9(2)	−0.5(1)	0.4(2)	0.07(6)	0.3(1)		4.67	8.22	13.8	12.8

inelastic components with energy lower than the energy of incoming neutrons (which for the wavelength of 2.36 Å is 14.68 meV). Moment values exceeding those expected from entropy calculations have also been observed with Mössbauer spectroscopy, where a maximum moment value of $\approx$1.5 μ_B based on a simple magnetic model has been estimated [11]. Tentative estimates from earlier neutron elastic scattering investigations also indicate moment values beyond the entropy prediction [10].

C. 2.2 T k_2 phase

For the k_2 state at $H = 2.2$ T, the best goodness of fit is obtained for the Γ_3 magnetic structure. The Yb3 moments retain their in-plane alignment along the [1 1 0] direction, while the Yb1 and Yb2 moments swap directions such that the Yb1 moment is aligned along [0 1 0] and Yb2 along

[1 0 0], hence breaking the CEF site-specific anisotropy. Attempting to force the moments to be aligned with their respective CEF anisotropy axes triples the χ^2 value, indicating that the proposed solution is preferred. As evidenced from Table III, the goodness of fit of the optimal fit is noticeably worse than any of the solutions for the other phases. This suggests that lower symmetry solutions should be tried with an improved data set.

The absent in-plane components of the k_2 propagation vector ensure that there is no amplitude modulation of the magnetic moments in the hexagonal plane, while the amplitude modulation along the $\hat{c}$-axis is maintained. The in-plane components of the Yb1, Yb2, and Yb3 individual sublattices are collinear and the canting between the different sublattices is 60/120°. The average moment amplitudes of Yb1, Yb2, and Yb3 are 0.8(1), 1.2(1), and 1.0(1) μ_B, thus lower than in the zero-field k_1 phase.

TABLE IV. Calculated magnetic quantities in (μ_B): Maximum moment components along the three crystal axes $\hat{a}$, $\hat{b}$, and $\hat{c}$ for each Yb$_l$ (l = 1,2,3), maximum moment amplitude $m_{i,max}$, average m_{av} and site-specific average $m_{i,av}$ moment amplitudes.

IRR	$m_{1,max}$	$m_{2,max}$	$m_{3,max}$	$m_{1,max}$	$m_{2,max}$	$m_{3,max}$	m_{av}	$m_{1,av}$	$m_{2,av}$	$m_{3,av}$
k_1 = (1/3 0 1/3), *H* = 0 T										
Γ_1	(−2.59(1), 0.3(1),−1.0(2))	(0.7(2),−1.8(1),0.2(2))	(−2.1(2),−2.1(2),0.9(2))	2.6(1)	1.7(1)	1.7(1)	1.62(3)	1.95(5)	1.24(4)	1.65(3)
Γ_2	(2.43(8),0.42(9),0.7(1))	(−0.6(1),−1.2(1),−0.5(2))	(−2.42(8),−2.7(1),0.7(2))	2.6(1)	1.2(1)	2.6(1)	1.59(2)	1.87(4)	1.04(4)	1.87(4)
k_2 = (0 0 0.32), *H* = 2.2 T										
Γ_3	(−0.1(2),−1.2(3),0.2(2))	(−1.5(2),0.0(3),0.63(9))	(1.2(3),1.5(3),−0.63(9))	1.2(2)	1.7(2)	1.5(2)	1.0(1)	0.8(1)	1.2(1)	1.0(1)
k_1 = (1/3 0 1/3), *H* = 3.9 T, Unconstrained										
Γ_1	(−1.10(8),−1.6(1),−0.1(1))	(−0.15(7),0.4(1),−0.72(9))	(−1.8(1),−0.2(1),0.4(1))	1.4(1)	0.9(1)	1.8(1)	0.90(1)	0.92(2)	0.58(2)	1.21(2)
Γ_2	(−1.43(9),−1.7(1),−0.6(1))	(0.10(5),−0.32(1),0.4(1))	(−1.43(9),0.3(2),0.3(1))	1.7(1)	0.42(8)	1.64(9)	0.93(2)	1.25(3)	0.40(3)	1.14(3)
k_1 = (1/3 0 1/3), *H* = 3.9 T, CEF constrained										
Γ_1	(0.64(6),0,0.1(1))	(0,0.5(1),0.2(1))	(−2.3(1),−1.74(7),0.3(1))	0.64(6)	0.5(1)	2.1(1)	0.81(1)	0.45(2)	0.38(3)	1.60(3)
Γ_2	(1.49(9),0,0.6(1))	(0,−0.8(1),−0.3(1))	(−1.49(9), −1.49(9),−0.6(1))	1.50(9)	0.8(1)	1.50(9)	0.94(2)	1.12(3)	0.61(3)	1.12(4)
k_3 = (0.195 0.195 0.38), *H* = 5.5 T										
Γ_2	(0.37(4),−0.53(6),0.08(7))	(−0.54(6),−0.5(1),0.4(1))	(−3.4(3),−3.3(3),−0.2(2))	0.78(6)	0.9(1)	3.3(1)	1.10(2)	0.51(1)	0.66(1)	2.12(3)

TABLE V. Complex basis functions of the physically irreducible representations for the three propagation vectors $\mathbf{k_1} = (\frac{1}{3}\ 0\ \frac{1}{3})$, $\mathbf{k_2} = (0\ 0\ 0.32)$, and $\mathbf{k_3} = (0.195, 0.195, 0.380)$.

IRR	BV	Yb1 (0.58,0,0)	Yb2 (0,0.58,0)	Yb3 (0.42, 0.42, 0)	
		Re	Re	Re	Im
$\mathbf{k_1} = (1/3\ 0\ 1/3)$					
Γ_2	Ψ_1	(1.00, 0.00, 0.00)	(0.00, 0.00, 0.00)	(0.50, 0.50, 0.00)	(0.87, 0.87, 0.00)
	Ψ_2	(0.00, 1.00, 0.00)	(0.00, 0.00, 0.00)	(0.00,-0.50, 0.00)	(0.00,-0.87, 0.00)
	Ψ_3	(0.00, 0.00, 1.00)	(0.00, 0.00, 0.00)	(0.00, 0.00, 0.50)	(0.00, 0.00, 0.87)
	Ψ_4	(0.00, 0.00, 0.00)	(0.00, 1.00, 0.00)	(0.00, 0.00, 0.00)	(0.00, 0.00, 0.00)
	Ψ_5	(1.00, 0.00, 0.00)	(0.00, 0.00, 0.00)	(-0.50,-0.50, 0.00)	(-0.87,-0.87, 0.00)
	Ψ_6	(0.00, 1.00, 0.00)	(0.00, 0.00, 0.00)	(0.00, 0.50, 0.00)	(0.00, 0.87, 0.00)
	Ψ_7	(0.00, 0.00, 1.00)	(0.00, 0.00, 0.00)	(0.00, 0.00, -0.50)	(0.00, 0.00,-0.87)
	Ψ_8	(0.00, 0.00, 0.00)	(-1.00,-0.50, 0.00)	(0.00, 0.00, 0.00)	(0.00, 0.00, 0.00)
	Ψ_9	(0.00, 0.00, 0.00)	(0.00, 0.00, 1.00)	(0.00, 0.00, 0.00)	(0.00, 0.00, 0.00)
Γ_1	Ψ_1	(1.00, 0.00, 0.00)	(0.00, 0.00, 0.00)	(0.00, 0.00, 0.00)	(0.00, 0.00, 0.00)
	Ψ_2	(0.00, 1.00, 0.00)	(0.00, 0.00, 0.00)	(0.00, 0.00, 0.00)	(0.00, 0.00, 0.00)
	Ψ_3	(0.00, 0.00, 1.00)	(0.00, 0.00, 0.00)	(0.00, 0.00, 0.00)	(0.00, 0.00, 0.00)
	Ψ_4	(0.00, 0.00, 0.00)	(0.00, 0.00, 0.00)	(1.00, 1.00, 0.00)	(1.73, 1.73, 0.00)
	Ψ_5	(0.00, 0.00, 0.00)	(0.00, 0.00, 0.00)	(-1.00, 0.00, 0.00)	(-1.73, 0.00, 0.00)
	Ψ_6	(0.00, 0.00, 0.00)	(0.00, 0.00, 0.00)	(0.00, 0.00,-1.00)	(0.00, 0.00,-1.73)
	Ψ_7	(0.00, 0.00, 0.00)	(0.00, 1.00, 0.00)	(0.00, 0.00, 0.00)	(0.00, 0.00, 0.00)
	Ψ_8	(0.00, 0.00, 0.00)	(-1.00,-1.00, 0.00)	(0.00, 0.00, 0.00)	(0.00, 0.00, 0.00)
	Ψ_9	(0.00, 0.00, 0.00)	(0.00, 0.00, 1.00)	(0.00, 0.00, 0.00)	(0.00, 0.00, 0.00)
$\mathbf{k_2} = (0\ 0\ 0.32)$					
Γ_1	Ψ_1	(0.50, 1.00, 0.00)	(-1.00,-0.50, 0.00)	(0.50,-0.50, 0.00)	(0.00, 0.00, 0.00)
Γ_2	Ψ_1	(1.00, 0.00, 0.00)	(0.00, 1.00, 0.00)	(-1.00,-1.00, 0.00)	(0.00, 0.00, 0.00)
	Ψ_2	(0.00, 0.00, 1.00)	(0.00, 0.00, 1.00)	(0.00, 0.00, 1.00)	(0.00, 0.00, 0.00)
Γ_3	Ψ_1	(1.00, 0.00, 0.00)	(0.00,-0.50, 0.00)	(0.50, 0.50, 0.00)	(0.00, 0.00, 0.00)
	Ψ_2	(0.00, 0.00, 0.00)	(-1.00,-0.50, 0.00)	(-0.50, 0.50, 0.00)	(0.00, 0.00, 0.00)
	Ψ_3	(0.00, 0.00, 0.00)	(0.00, 0.00, 1.00)	(0.00, 0.00,-1.00)	(0.00, 0.00, 0.00)
	Ψ_4	(0.00, 0.00, 0.00)	(0.00,-1.00, 0.00)	(-1.00,-1.00, 0.00)	(0.00, 0.00, 0.00)
	Ψ_5	(0.50, 1.00, 0.00)	(0.50, 0.25, 0.00)	(-0.25, 0.25, 0.00)	(0.00, 0.00, 0.00)
	Ψ_6	(0.00, 0.00, 1.00)	(0.00, 0.00,-0.50)	(0.00, 0.00,-0.50)	(0.00, 0.00, 0.00)
$\mathbf{k_3} = (0.195\ 0.195\ 0.38)$					
Γ_1	Ψ_1	(1.00, 0.00, 0.00)	(0.00,-1.00, 0.00)	(0.00, 0.00, 0.00)	(0.00, 0.00, 0.00)
	Ψ_2	(0.00, 1.00, 0.00)	(-1.00, 0.00, 0.00)	(0.00, 0.00, 0.00)	(0.00, 0.00, 0.00)
	Ψ_3	(0.00, 0.00, 1.00)	(0.00, 0.00,-1.00)	(0.00, 0.00, 0.00)	(0.00, 0.00, 0.00)
	Ψ_4	(0.00, 0.00, 0.00)	(0.00, 0.00, 0.00)	(1.00,-1.00, 0.00)	(0.00, 0.00, 0.00)
	Ψ_5	(0.00, 0.00, 0.00)	(0.00, 1.00, 0.00)	(1.00, 1.00, 0.00)	(0.00, 0.00, 0.00)
	Ψ_6	(0.00, 0.00, 0.00)	(-1.00,-1.00, 0.00)	(0.00,-1.00, 0.00)	(0.00, 0.00, 0.00)
	Ψ_7	(0.00, 0.00, 0.00)	(0.00, 0.00, 1.00)	(0.00, 0.00,-1.00)	(0.00, 0.00, 0.00)
Γ_2	Ψ_1	(1.00, 0.00, 0.00)	(0.00, 1.00, 0.00)	(0.00, 0.00, 0.00)	(0.00, 0.00, 0.00)
	Ψ_2	(0.00, 1.00, 0.00)	(1.00, 0.00, 0.00)	(0.00, 0.00, 0.00)	(0.00, 0.00, 0.00)
	Ψ_3	(0.00, 0.00, 1.00)	(0.00, 0.00, 1.00)	(0.00, 0.00, 0.00)	(0.00, 0.00, 0.00)
	Ψ_4	(0.00, 0.00, 0.00)	(0.00, 0.00, 0.00)	(-1.00,-1.00, 0.00)	(0.00, 0.00, 0.00)
	Ψ_5	(0.00, 0.00, 0.00)	(0.00, 0.00, 0.00)	(0.00, 0.00, 1.00)	(0.00, 0.00, 0.00)
	Ψ_6	(0.00, 0.00, 0.00)	(0.00, 1.00, 0.00)	(-1.00,-1.00, 0.00)	(0.00, 0.00, 0.00)
	Ψ_7	(0.00, 0.00, 0.00)	(-1.00,-1.00, 0.00)	(0.00, 1.00, 0.00)	(0.00, 0.00, 0.00)
	Ψ_8	(0.00, 0.00, 0.00)	(0.00, 0.00, 1.00)	(0.00, 0.00, 1.00)	(0.00, 0.00, 0.00)

D. 3.9 T phase with re-entrant $\mathbf{k_1}$ propagation vector

The $\mathbf{k_1}$ propagation vector re-enters at magnetic fields between 3 and 4.8 T. Nonconstrained refinements with both the Γ_1 and Γ_2 IRRs yield solutions with moments deviating from the CEF anisotropy axes. Forcing the Yb1 and Yb2 moments to be along their respective anisotropy axes results in slightly worse goodnesses of fit and we thus present all four solutions in Table III. Overall, the Γ_1 IRR results in slightly better goodnesses of fit for both the CEF-constrained and nonconstrained refinements compared to the Γ_2 refinements. Both solutions
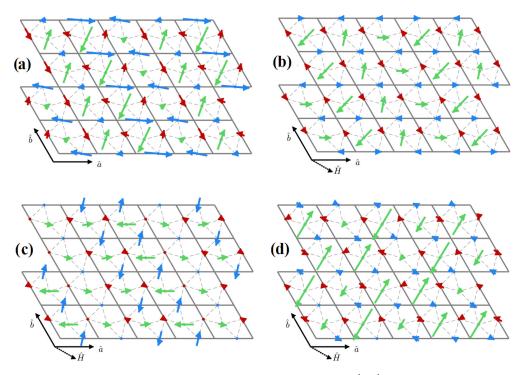
FIG. 5. A $(t_x, t_y, 0)$ layer of the magnetic structures for (a) 0-T Γ_2 solution with $\mathbf{k_1} = (\frac{1}{3}\ 0\ \frac{1}{3})$, (b) 3.9-T Γ_3 solution with $\mathbf{k_1} = (\frac{1}{3}\ 0\ \frac{1}{3})$ and enforced CEF anisotropy for Yb1 and Yb2 moments, (c) 3.9-T unconstrained Γ_1 solution with $\mathbf{k_1} = (\frac{1}{3}\ 0\ \frac{1}{3})$, and (d) 5.5-T Γ_2 solution with $\mathbf{k_3} = (0.195\ 0.195\ 0.38)$. The magnetic moments of Yb1, Yb2, and Yb3 are coloured blue, red, and green, respectively. The magnetic field direction is [1 –1 0] in (b), (c), and (d).

are shown in Figs. 5(b) and 5(c), respectively. For both Γ_1 solutions an unequal distribution of moment amplitudes is obtained. The average values are presented in Table IV. The unconstrained solution strongly breaks the CEF anisotropy as seen by the Yb1 and Yb3 moments being oriented primarily along [1 1 0] and [1 0 0], respectively. There is, thus, a large variance in the proposed magnetic structures, which all possess similar goodnesses of fit. This results in a certain ambiguity in the magnetic arrangement of the c phase.

Both the constrained and unconstrained solutions exhibit decreased antiferromagnetic contributions, as gauged from the average magnetic-moment amplitudes of 0.81(1) μ_B and 0.90(1) μ_B compared to the zero-field solution with an average antiferromagnetic moment of 1.62(3) μ_B. The decrease in the antiferromagnetic contribution may be compensated by an increasing ferromagnetic contribution in the c phase as shown in Figs. 2 and 6.

E. High-field $\mathbf{k_3}$ phase

The d-phase propagation vector $\mathbf{k_3} = (0.195\ 0.195\ 0.38)$ is observed at 5.5 T, above the suggested bicritical point at $H_{\text{crit}}^{ab} \approx 4.5$ T. The best model, corresponding to the Γ_2 IRR, results in an amplitude-modulated structure with the in-plane components of the Yb1, Yb2, and Yb3 magnetic moments directed along their CEF anisotropy axes. In this structure, the average increase of magnetic moments is small when compared to the 3.9-T $\mathbf{k_1}$ phase, but a stronger difference between the Yb3 moment and the Yb1 and Yb2 moments is apparent. The Yb3 moments reach on average 2.12(3) μ_B, while the remaining 2/3 of the moments are less than 1 μ_B,

i.e., on average 0.51(1) μ_B/Yb1 and 0.66(1) μ_B/Yb2. This difference might be partly compensated by the ferromagnetic component, which is significant. However, its site variation has not been addressed yet.

IV. DISCUSSION

We presented results of a series of neutron diffraction experiments on YbAgGe single crystals performed in the mK regime in zero and under magnetic fields applied in the hexagonal plane. We determined models of magnetic arrangements for the zero-field a and the low-field b phases with the previously reported $\mathbf{k_1}$ and $\mathbf{k_2}$ propagation vectors. We discovered the $\mathbf{k_1}$ propagation vector in phase c at 3.9 T and suggested the associated magnetic structure. The propagation vector in phase d appearing above the critical field $H_{\text{crit}}^{ab} \approx 4.5$ T is found to be $\mathbf{k_3} = (0.195\ 0.195\ 0.380)$ and the corresponding magnetic arrangement is determined. The field-temperature extent of these four regions agrees very well with the H-T phase diagrams established by extensive measurements of magnetization, specific heat, thermal expansion, magnetostriction, electrical resistivity, Hall effect, and thermoelectric power [1–5,14,17,18].

Qualitatively, the low-field features of the magnetic phase diagram of YbAgGe (phases a, b, and c) follow the general trend for rare-earth systems. In zero-field cooling, the incommensurate magnetic $\mathbf{k_2}$ order appears first. It locks into the commensurate $\mathbf{k_1}$ state at low temperatures and then re-enters upon application of magnetic field. The mean-field model of Ref. [22] accounts for these features, assigning their origin to exchange interactions, while crystal electric fields impose
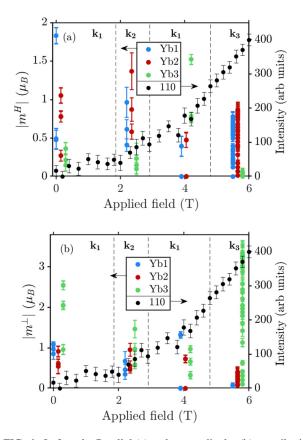
FIG. 6. Left scale: Parallel (a) and perpendicular (b) contribution of the magnetic moment with respect to the applied field $H_{[1-10]}$. All modulated moment amplitudes within the magnetic unit cell of the best refined models have been included, explaining the multiple values reported for Yb1, Yb2, and Yb3 at each applied field. For visual clarity, the moment amplitude for Yb2 and Yb3 have been shifted slightly on the x axis. The field values of the Yb1 moments correspond to the actual field values. Right scale: Black circles follow the field-dependent integrated intensity of the (110) nuclear peak.

the local moment directions and the exact positions of the magnetic phase boundaries.

Although the low-field phase diagram of YbAgGe retains all these features, there is still a significant deviation from this common trend. Usually, equal-moment collinear structures are favored at low temperatures. In YbAgGe, all magnetic structures, including the low-temperature zero-field one, are amplitude modulated. It is not clear to what extent this is dictated by geometrical frustration in the kagome layers or by the proximity to the non-Fermi-liquid state. However, it is apparent that the interplay of the CEF anisotropy of the three Yb sites, the applied magnetic field, and the frustrated exchange interactions play a significant role.

The enhanced moment amplitudes for Yb3 in the phases c and d are likely related to its local [1 1 0] anisotropy direction. [1 1 0] is perpendicular to the applied-field direction and thus the field has no effect on the ordering of this sublattice. In contrast, the Yb1 and Yb2 magnetic sites are strongly influenced by the competition of the local CEF anisotropy and magnetic-field direction, such that they align either along their CEF axes (phases a and d) or normal to them (phases b and c). Remarkably, we observe significant $\hat{c}$ components in all

proposed magnetic arrangements, which is hard to reconcile with the suggested CEF ground state of the Yb^{3+} ions [9]. Even so, in all these cases the in-plane components of the moments retain a 60 or 120 degrees canting with respect to the neighboring spins of the other two sublattices. Such a canted arrangement is reminiscent of the classical ground state of Heisenberg kagome antiferromagnets [23]. This implies that the interaction between the first neighbors in YbAgGe is antiferromagnetic and substantial.

A better understanding of the complex metamagnetic behavior in YbAgGe requires insight into Ruderman-Kittel-Kasuya-Yosida (RKKY) exchange interactions of this material. This is challenging, as the Fermi surface of YbAgGe is anisotropic [2] and no reliable calculation of the electronic structure is available at this point. We attempt here a rough estimate of RKKY, simplifying the YbAgGe Fermi surface as being spherical and characterized by a single k_F value, which we estimated from bulk measurements [18].

Given a carrier concentration of $n = 3.1 \times 10^{21}$ cm^{-3}, which has been normalized with the unit-cell volume and number of Yb ions, $n^* = n \times 178 \times 10^{-24}/3$, we calculate

$$k_F = (n^* \times 3\pi^2)^{1/3} = 1.76 \text{ Å}^{-1} \quad (3)$$

Figure 7 presents the distance dependence of the RKKY interaction calculated as $J(k_F) = C \times F(2k_F r)$, where C is a normalization constant and $F(x) = (\sin x - x \cos x)/x^4$. According to this model the RKKY exchange can be approximated by the bilinear AF in-plane exchange couplings up to fourth-nearest neighbor and a mixture of ferromagnetic and antiferromagnetic out-of-plane exchange couplings.

We note that this simplified picture has to be taken with caution. The propagation vectors identified for YbAgGe are not typical for the rest of the RAgGe family and are even more distant to other kagome or distorted-kagome compounds. The ordering vector $\mathbf{k_1} = (\frac{1}{3} 0 \frac{1}{3})$ is very rarely observed in particular. We performed a Monte Carlo sampling of a Heisenberg Hamiltonian with up to twelve isotropic nearest-neighbor exchanges based on the generalized Luttinger-Tisza method [24] and detected only a few tiny pockets where the $\mathbf{k_1}$ structure would be energetically stable. Thus presumably a more complex Hamiltonian that includes anisotropic exchanges, has to be considered.

Because the anomalous Hall effect was observed at the c–d phase boundary [25], we inspected the topology of the determined magnetic structures by calculating the average scalar spin chirality,

$$\chi = 1/N \sum_j \mathbf{S_1} \cdot (\mathbf{S_2} \times \mathbf{S_3}). \quad (4)$$

Here, the sum runs over all j triangles formed by the Yb1, Yb2, and Yb3 moments in the magnetic unit cell. For the proposed 0-T (phase a), 2.2-T (phase b), and 5.5-T (phase d) models, the average chirality is zero within errors. In contrast, the two Γ_1 3.9-T solutions (phase c) reveal a finite average chirality of 0.3(1) and –0.61(3), respectively. It is possible that the anomalous Hall effect in YbAgGe is induced by the spin chirality, similar to the frustrated-noncollinear-triangular-lattice Mn_3Sn [26] and $Fe_{1.3}Sb$ [27]. Thus other nontrivial properties such as topological band crossing and existence of
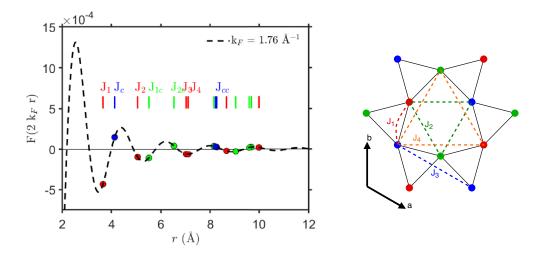
FIG. 7. An estimate of the RKKY exchange distance dependence (dashed line) plotted alongside markers for the Yb-Yb distances. J_1-J_4 are the in-plane nearest-neighbor exchanges, shown also in the right figure, J_c, J_{cc} are exchanges in the $\hat{c}$ direction across one and two unit cells, respectively.

topological fermions may be expected in YbAgGe. Also, the scalar chirality may be driven by chiral fluctuations triggered by frustrated interactions, as is the case in the kagome-compound YMn_6Sn_6 [28].

The high-field features of the phase diagram (phases c and d) merit further discussion. In phase d, the average moment amplitude of the Yb3 ion significantly exceeds (by almost four times) the values of the other two ions. This questions the role of the Yb1 and Yb2 local moments, i.e., whether they strongly fluctuate due to frustration, or whether their values are reduced due to the hybridization of $4f$ and conduction electrons. To establish a site-specific variation of the hybridization for Yb1/Yb2 and Yb3, these sites should become different under magnetic field. This could happen, if structural transition splitting the 3(f) site of Yb into two sites takes place. A possible hint of structural change is seen in the magnetostriction data [5], however no signature of an abrupt change in the crystal structure is observed in our neutron diffraction data. Thus, the dynamic coupling between the crystal lattice and the magnetic degrees of freedom has to be inspected carefully. A coupling between the CE levels and the phonons may be one possibility, which has been seen in $CeAuAl_3$ for instance [29]. A strong coupling between CE levels and lattice vibrations would affect the elastic constants of YbAgGe, and has indeed been observed in previous reports [6]. Here, the softening of the elastic constants at H_{crit} was attributed to the broadening of the $4f$ level to gain Zeeman energy, which in turn yields a suppressed heavy-fermion behavior. To confirm such a scenario, state-of-the-art *ab initio* electronic-structure calculations, a study of the Fermi surface evolution when crossing the BCP, or a verification of the magneto-elastic nature of the excitations are needed. Furthermore, numerous experimental results on YbAgGe show also evidence of non-Fermi-liquid behavior at the c-d phase boundary [5,7], pointing to a scenario in which the Yb1 and Yb2 moments are strongly reduced due to critical fluctuations. Here theoretical models that help to understand how the d-phase magnetic structure and/or its associated excitation spectrum result in a linear T dependence of the resistivity [3] are desired to make

further progress in clarifying which of the aforementioned scenarios is dominant.

The tuning of the bicritical point at $T = 0.3$ K and $H = 4.5$ T to zero temperature is another exciting area of research. The application of pressure or chemical substitution, may push the BCP towards a quantum BCP, and further to a field-induced quantum spin-liquid state [7]. Actually, even in not-optimally tuned YbAgGe, spin fluctuations may epitomize quantum spin-liquid-like character near Q = $\mathbf{k_3}$. A study of the dynamic spin correlations using inelastic neutron scattering would be valuable to distinguish which of the two scenarios—quantum fluctuations of a metallic spin liquid state or a magnetic site-specific Kondo screening—is realized in YbAgGe.

Finally, the possibility of magnetic order being associated with the e phase warrants further experimental investigation. The Fermi-liquid behavior of the f phase could be consistent with fully field-polarized Yb moments, which is not associated with any finite propagation vector. However, the phase boundary between the e and f phase indicates a different magnetic order in the e phase anticipating that a finite ordering vector could occur here. Therefore, it is salient to continue searching for the e-phase magnetic order either in the not-yet-explored part of reciprocal space or at $\mathbf{k} = (0, 0, 0)$.

[1] S. L. Bud'ko, E. Morosan, and P. C. Canfield, Phys. Rev. B **69**, 014415 (2004).

[2] S. L. Bud'ko, V. Zapf, E. Morosan, and P. C. Canfield, Phys. Rev. B **72**, 172413 (2005).

[3] P. G. Niklowitz, G. Knebel, J. Flouquet, S. L. Bud'ko, and P. C. Canfield, Phys. Rev. B **73**, 125101 (2006).

[4] E. Mun, S. L. Bud'ko, and P. C. Canfield, Phys. Rev. B **82**, 174403 (2010).

[5] G. M. Schmiedeshoff, E. D. Mun, A. W. Lounsbury, S. J. Tracy, E. C. Palm, S. T. Hannahs, J.-H. Park, T. P. Murphy, S. L. Bud'ko, and P. C. Canfield, Phys. Rev. B **83**, 180408(R) (2011).

[6] Y. Nakanishi, R. Kashiwazaki, K. Deto, F. Shichinomiya, M. Nakamura, H. Kubo, K. Umeo, T. Onimaru, T. Takabatake, and M. Yoshizawa, J. Phys.: Conf. Ser. **273**, 012011 (2011).

[7] Y. Tokiwa, M. Garst, P. Gegenwart, S. L. Bud'ko, and P. C. Canfield, Phys. Rev. Lett. **111**, 116401 (2013).

[8] B. Fåk, D. F. McMorrow, P. G. Niklowitz, S. Raymond, E. Ressouche, J. Flouquet, P. C. Canfield, S. L. Bud'ko, Y. Janssen, and M. J. Gutmann, J. Phys.: Condens. Matter **17**, 301 (2005).

[9] T. Matsumura, H. Ishida, T. J. Sato, K. Katoh, Y. Niide, and A. Ochiai, J. Phys. Soc. Jpn. **73**, 2967 (2004).

[10] B. Fåk, Ch. Rüegg, P. G. Niklowitz, D. F. McMorrow, P. C. Canfield, S. L. Bud'ko, Y. Janssen, and K. Habicht, Phys. B: Condens. Matter **378–380**, 669 (2006).

[11] P. Bonville, M. Rams, K. Królas, P. C. Canfield, J.-P. Sanchez, O. Trovarelli, and C. Geibel, Eur. Phys. J. B **55**, 77 (2007).

[12] H. Kubo, K. Umeo, K. Katoh, A. Ochiai, and T. Takabatake, J. Phys. Soc. Jpn. **79**, 064715 (2010).

[13] G. Zanicchi, D. Mazzone, V. Contardi, R. Marazza, G. Rambaldi, and D. Rossi, Gazz. Chim. Ital. **113**, 257 (1983).

[14] E. Morosan, S. L. Bud'ko, P. C. Canfield, M. S. Torikachvili, and A. H. Lacerda, J. Magn. Magn. Mater. **277**, 298 (2004).

[15] E. Morosan, S. L. Bud'ko, and P. C. Canfield, Phys. Rev. B **71**, 014445 (2005).

[16] K. Zhao, H. Deng, H. Chen, K. A. Ross, V. Petříček, G. Günther, M. Russina, V. Hutanu, and P. Gegenwart, Science **367**, 1218 (2020).

[17] K. Katoh, Y. Mano, K. Nakano, G. Terui, Y. Niide, and A. Ochiai, J. Magn. Magn. Mater. **268**, 212 (2004).

[18] S. L. Bud'ko, E. Morosan, and P. C. Canfield, Phys. Rev. B **71**, 054408 (2005).

[19] Y. Tokiwa, A. Pikul, P. Gegenwart, F. Steglich, S. L. Bud'ko, and P. C. Canfield, Phys. Rev. B **73**, 094435 (2006).

[20] P. C. Canfield, Rep. Prog. Phys. **83**, 016501 (2019).

[21] J. Rodríguez-Carvajal, Phys. B: Condens. Matter **192**, 55 (1993).

[22] D. Gignoux and D. Schmitt, Phys. Rev. B **48**, 12682 (1993).

[23] J. T. Chalker, P. C. W. Holdsworth, and E. F. Shender, Phys. Rev. Lett. **68**, 855 (1992).

[24] J. M. Luttinger and L. Tisza, Phys. Rev. **70**, 954 (1946).

[25] H. Ishizuka and N. Nagaosa, Sci. Adv. **4**, eaap9962 (2018).

[26] S. Nakatsuji, N. Kiyohara, and T. Higo, Nature (London) **527**, 212 (2015).

[27] Y. Shiomi, M. Mochizuki, Y. Kaneko, and Y. Tokura, Phys. Rev. Lett. **108**, 056601 (2012).

[28] N. J. Ghimire, R. L. Dally, L. Poudel, D. C. Jones, D. Michel, N. T. Magar, M. Bleuel, M. A. McGuire, J. S. Jiang, J. F. Mitchell, J. W. Lynn, and I. I. Mazin, Sci. Adv. **6**, eabe2680 (2020).

[29] P. Čermák, A. Schneidewind, B. Liu, M. M. Koza, C. Franz, R. Schönmann, O. Sobolev, and C. Pfleiderer, Proc. Natl. Acad. Sci. USA **116**, 6695 (2019).